Materials Research. 2026; 29: e20250614
DOI: https://doi.org/10.1590/1980-5373-MR-2025-0614

Wire Arc Additive Manufacturing Through the Gas Tungsten Arc Welding Process for ER 310 and ER 70S-6 Alloys

Carlos Antônio Ferreira[a] **,** ***Lirio Schaeffer***[b] **,** ***Pedro Henrique Menegaro Possamai***[a]* **,**
Anderson Daleffe[a] **,** ***Henrique Cechinel Casagrande***[a] **,** ***Luciano Dagostin Bilessimo***[a]

[a]*SATC - Educação e Negócios, Criciúma, SC, Brasil.*
[b]*Universidade Federal do Rio Grande do Sul (UFRGS), Departamento de Engenharia Metalúrgica (DEMET), Porto Alegre, RS, Brasil.*

Received: September 08, 2025; Revised: May 05, 2026; Accepted: July 08, 2026

Metal Additive Manufacturing (AM) via Wire Arc Additive Manufacturing (WAAM) has gained prominence as a viable alternative for the fabrication of complex metallic components. In this study, the feasibility of the dual-wire Gas Tungsten Arc Welding (GTAW) process was evaluated for the production of parts using ER310 and ER70S-6 consumables, employing an IMC DIGIPLUS A7 power source integrated with a Cartesian motion system. Characterization included tensile testing, microhardness measurements, and metallographic analysis. Microstructural analyses, combined with measurements performed on metallographic images, revealed a mean grain size of 3.04 µm, characteristic of the microstructural refinement promoted by the high cooling rates inherent to the WAAM process. Tensile results indicated that the material deposited with the ER310 + ER70S-6 combination exhibited a mean ultimate tensile strength ranging from 248 to 333 MPa and elongation values between 9 and 10%, which are lower than those observed for deposits produced solely with ER310 (320 – 430 MPa) and ER70S-6 (393 – 438 MPa), yet with comparable or superior ductility. The mean microhardness of the hybrid material was 233 ± 20 HV, significantly higher than that of ER310 (191 ± 8 HV) and ER70S-6 (161 ± 23.7 HV) single-wire deposits, evidencing the effect of consumable combination on the hardening behavior of the deposited material. Overall, the results demonstrate that the dual-wire GTAW process enables the production of a material exhibiting a balanced combination of mechanical strength, ductility, and hardness, alongside a stable microstructure and the absence of macroscopic defects, thereby confirming the potential of WAAM for engineering applications.

Keywords: *Wire arc additive manufacturing, Gas tungsten arc welding, Double-wire, Dissimilar alloys.*

1. Introduction

The metalworking industry continuously seeks greater productivity combined with quality improvement and cost reduction[1,2]. In this context, metal Additive Manufacturing (AM) has advanced significantly, with Wire Arc Additive Manufacturing (WAAM) standing out as a prominent approach, employing an electric arc to melt a wire feedstock and deposit material layer by layer along a programmed trajectory[3]. This technology enables greater design freedom in the fabrication of complex geometries compared to conventional manufacturing methods[4,5].

Current industrial demands include the production of complex structures with minimal material waste, high process efficiency, and satisfactory mechanical performance. Accordingly, AM has gained increasing prominence by enabling material savings, cost reduction, and improvement of final component properties[6,7].

The WAAM process has attracted considerable industrial and academic attention due to its capacity to employ conventional welding equipment and consumables for the fabrication of complex geometries through layer-by-layer wire fusion deposition. Compared to powder-based techniques employing energy sources such as laser and electron beam, WAAM offers lower costs and high deposition rates[8-10]. It is classified as a Directed Energy Deposition (DED) process and may employ welding methods such as Gas Metal Arc Welding (GMAW) and Gas Tungsten Arc Welding (GTAW), both of which are based on electric arc with shielding gas protection[1].

WAAM enables the fabrication of components with adequate surface finish and high deposition rates, reaching up to 5 kg/h for AISI 316L and 2.5 kg/h for Ti-6Al-4V. The selection of a specific process variant depends on the application requirements and may include Cold Metal Transfer (CMT), Plasma Arc Welding (PAW), and GTAW, each exhibiting distinct deposition capabilities. These results highlight the viability of WAAM as an alternative to traditional manufacturing processes such as casting and forging[11,12].

AM is an innovative manufacturing approach based on layer-by-layer material deposition, providing superior efficiency in the production of metallic components[13,14].

*e-mail: pedropossamai@hotmail.com
Associate Editor: Aloisio Klein.
Editor-in-Chief: Luiz Antonio Pessan.

Within the WAAM framework, the GTAW process is particularly noteworthy for its arc stability and low oxidation levels, making it well suited for the deposition of stainless steels and for AM applications[15,16].

Among the existing challenges within the WAAM process, the most demanding is the development and production of defect-free components with satisfactory physical, mechanical, and metallurgical properties that meet engineering requirements[17,18]. Fundamental characteristics of AM include the reduction in the number of manufacturing steps and operations, material savings, and the possibility of unprecedented geometry material combinations[19].

In GTAW-based AM, the arc is established between the non-consumable tungsten electrode and the substrate, generating a melt pool on the substrate surface. The filler wires are fed into the molten pool through its leading edge, where they are melted and deposited onto the substrate surface. In this configuration, the heat generated at the anode is used exclusively to sustain the melt pool on the substrate surface, which is attributed to the inherently low energy efficiency of the GTAW-WAAM process[6,20].

The GTAW process exhibits high energy efficiency (~90%) and is suitable for the fabrication of components, particularly thin-walled structures, including applications involving dissimilar materials[8,21,22]. Furthermore, multi wire feeding systems can be employed to enable the production of functionally graded materials, leveraging the stable arc established between the tungsten electrode and the base material[8,21,23,24].

For component production via WAAM, it is essential to correlate welding parameters with bead geometry (width and height), as these parameters govern layer-by-layer deposition and determine the final wall thickness of the component[25].

The authors in[1], in their investigation of dual WAAM, highlight that this process involves complex force interactions governed by the welding parameters, giving rise to three primary metal transfer modes: short circuit, globular, and spray. These modes are directly correlated with the energy input applied, ranging from short circuit transfer associated with the lowest energy levels to spray transfer, which is achieved at higher welding currents and results in a process with greater heat input.

The authors in[26], in their research on WAAM, report that only a limited number of studies on multi-material WAAM have been conducted. Among them, Kumar et al.[27] investigated the combination of SS321 stainless steel and Inconel 625, finding that microstructural features varied along the build direction, with equiaxed and columnar dendrites observed in the SS321 layers, while the Inconel 625 layers consisted predominantly of fine columnar and cellular dendrites. Ahsan, Md Rumman Ul et al.[28] combined low-carbon steel and 316L stainless steel, identifying an increase in hardness at the transition zone. In a subsequent study, Ahsan, Md R.U. et al.[29] also investigated the influence of heat treatment on such bimetallic structures, finding that the failure location shifted from the low-carbon steel side to the stainless-steel side following thermal processing.

Given the growing interest in AM, a thorough understanding of the deposition process and the resulting material characteristics becomes essential when employing welding-based methods. In this context, the GTAW process was selected for AM due to its high arc stability and precise control over heat input fundamental attributes for layer-by-layer deposition in the WAAM process. Furthermore, relatively few studies have addressed GTAW-based WAAM. Chaturvedi et al.[30] present a review of different techniques employed in WAAM, highlighting the scarcity of research specifically focused on GTAW. Yang et al.[31] employed a hybrid process combining GTAW and GMAW, in which dual electrode gas metal arc welding (DE-GMAW) was used for the fabrication of thin and narrow metallic wall components. The authors in[32-34] report that, compared to GMAW and CMT based processes, GTAW exhibits greater arc stability and lower deposition rates characteristics that favor the formation of layers with improved surface finish. In GTAW-based WAAM, the arc length remains stable under variations in heat input, while the deposition rate is independently controlled by the wire feed speed, resulting in greater process controllability compared to GMAW and CMT based approaches[35].

Although multi-material WAAM approaches and dual-wire feeding strategies have been previously reported, the vast majority of existing studies are based on GMAW or plasma arc processes. Moreover, even in cases involving dissimilar wire combinations, the literature tends to address material systems with lower compositional contrast or focuses predominantly on process feasibility.

In the present work, the novelty is reinforced by the use of a specific dissimilar material system combining ER310 and ER70S-6 filler wires, which exhibit significant differences in chemical composition and phase formation potential. This selection is not straightforward, as it involves the interaction between a material rich in austenite-stabilizing elements (Cr and Ni) and a low-carbon steel, resulting in a system highly sensitive to dilution mechanisms and melt pool dynamics[36,37].

In this context, the primary scientific contribution lies not merely in the application of dual-wire GTAW-WAAM, but in the exploration of in-situ controlled alloying arising from this dissimilar combination, enabling an assessment of how the wire feeding strategy directly influences the final chemical composition, phase formation (metallic matrix and carbides), and wear performance.

Specifically, this work establishes a correlation among: (I) the wire feeding strategy, (II) the resulting chemical composition, (III) microstructural evolution, and (IV) functional properties. This integrated approach broadens the understanding of the interaction mechanisms between dissimilar materials in GTAW-based WAAM, a topic that remains insufficiently explored in the literature.

Thus, the specific combination of consumables, combined with process control and systematic analysis of processing, microstructure and property relationships, defines the originality and scientific relevance of this study.

For validation of the obtained results, Optical Emission Spectroscopy (OES), mechanical tensile testing, Vickers Hardness (HV) measurements, and metallographic analyses by optical microscopy (OM) and Scanning Electron Microscopy (SEM) will be performed, complemented by Energy Dispersive Spectroscopy (EDS) and X-Ray Diffraction (XRD). These techniques will enable the correlation of chemical composition, microstructural features, and mechanical properties of the deposited material, ensuring a comprehensive evaluation of the performance of the developed system.

2. Experimental Procedures

In order to produce the manufactured components, an integration between a GTAW welding machine and a Computer Numerical Control (CNC) coordinate machine was carried out, with the purpose of enabling the fabrication of additively manufactured parts. For the present study, a semi-automatic welding machine, model DIGIPLUS A7, manufactured by IMC, was employed. The manufacturing system operates via CNC, executing movements along three axes, including the motion control of the welding torch, which is responsible for performing the layer-by-layer material deposition, thereby enabling a uniform material flow, as illustrated in Figure 1.

The shielding gas employed was argon (Ar), providing the protective atmosphere required for the GTAW welding process. Regarding the process parameters, identical settings were adopted for both consumables, as illustrated in Table 1; the selected parameters were chosen within the range recommended by the consumable manufacturer.

The programming for the production of the manufactured components was performed manually within the software environment, using G-code programming language for Mach3 a software commonly employed for programming machine tools such as CNC machining centers and lathes. It is noteworthy that this technique enables a constant material deposition height and consistent torch motion, thereby ensuring homogeneity in material deposition and promoting localized fusion along the fabricated component. For the present study, a parallel deposition strategy was adopted, in which the torch performs a deposition pass and returns to the beginning of the bead before initiating the subsequent layer, as observed in Figure 2, item B. Subsequently, the torch travel speed was determined and controlled through programming. Taking into account the target component geometry, Figure 2, item A illustrates the initial stage of wall fabrication, during which parameter adjustments were performed.

Table 1. Operational parameters employed in the GTAW process, including electrical and geometrical variables that influence arc stability, deposition rate, and the quality of the deposited layers.

Voltage (V)	14.8
Current (A)	180
Wire feed speed (m/min)	1.3
Gas flow rate (l/min)	12
Torch travel speed (mm/min)	150
Wire diameter (mm)	1.2

Source: Author (2026).

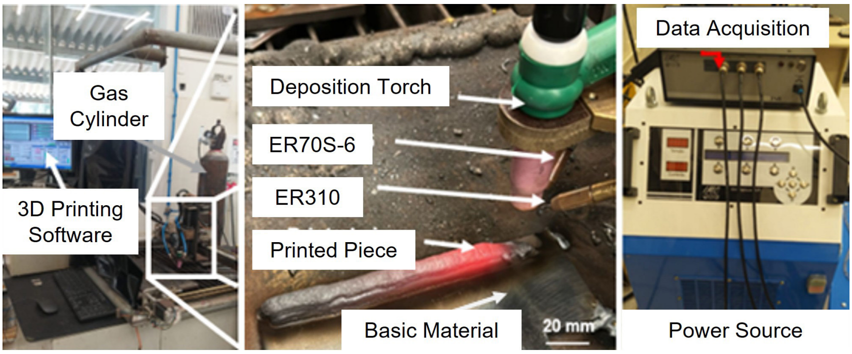

Figure 1. Wire arc additive manufacturing equipment based on the gas tungsten arc welding process, highlighting the non-consumable electrode torch, the material feeding system, and the layer-by-layer deposition control employed in the fabrication of metallic structures.

Source: Adapted from Silva et al.[5].

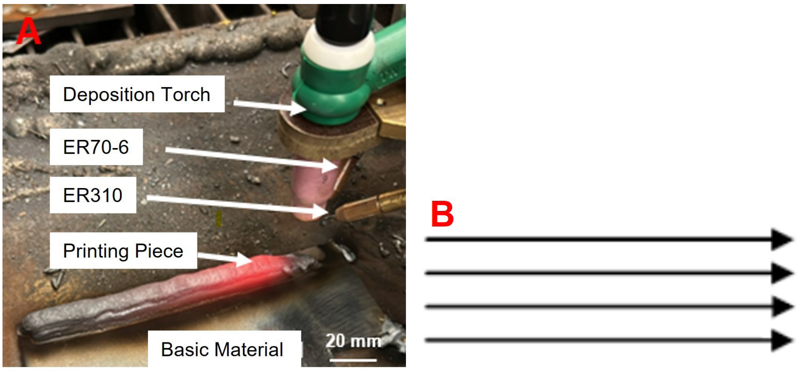

Figure 2. Metallic wall obtained by additive manufacturing following process parameter adjustment via GTAW; (B) representation of the parallel-path deposition strategy employed during the build process.

Source: Author (2026).

2.1. Optical emission spectroscopy

Chemical characterization by Optical Emission Spectrometry (OES) was performed using a BRUKER Q2 ION spectrometer, operating at 400 W for 30 s. Initially, the sample was sectioned using a Struers MESOTOM metallographic cutter. Subsequently, machining was carried out on a Romi U30 milling machine, followed by surface grinding on a Mello P36 surface grinder, with the purpose of reducing surface roughness. It is worth noting that this analysis was conducted after the additive manufacturing of the sample.

2.2. Tensile testing

Tensile tests were conducted at a crosshead displacement rate of 5 mm/min, using an InterMetric GR173 universal testing machine with a nominal capacity of 200 kN. The specimens were initially prepared by machining on a Romi U30 milling machine and subsequently subjected to surface grinding on a Mello P36 surface grinder to reduce surface roughness. The samples were then cut in accordance with the requirements of ASTM E8 standard[38], employing an AMADA FLC 3015 AJ laser cutting machine. In order to investigate the anisotropic behavior of the WAAM-deposited material, specimens were extracted in three distinct orientations relative to the deposition track direction (0°, 45°, and 90°). For each condition, tests were performed in triplicate, ensuring the statistical reliability of the mechanical results.

2.3. Microstructural characterization

Scanning Electron Microscopy (SEM) and Energy Dispersive Spectroscopy (EDS) analyses were performed on a Zeiss EVO MA 10 microscope, operating at 10 kV and equipped with a tungsten filament. Microstructural phase revelation was carried out by chemical etching with Vilella's reagent, applied for 180 s, for both SEM and OM analyses. OM observations were performed on an Olympus SC30 microscope.

The samples were initially sectioned using a Struers MESOTOM metallographic cutter and subsequently extracted along the deposition direction. Metallographic preparation included sequential grinding with abrasive papers of 80, 120, 200, 320, 400, 600, and 1200 grit, followed by polishing on a Fortel PFL polishing machine using alumina suspension with a mean particle size of 1 μm diluted in water.

2.4. Grain size

Sample preparation began with sectioning using a Struers MESOTOM metallographic cutter. Subsequently, progressive surface material removal was performed through sequential grinding with abrasive papers of 80, 120, 200, 320, 400, 600, and 1200 grit. Following this stage, the sample was subjected to polishing on an AROTEC AROPOL polishing machine using alumina suspension with a mean particle size of 1 μm diluted in water. With the surface adequately prepared, the sample was analyzed by OM on an Olympus SC30 microscope. Grain size quantification was carried out using PRECiV Pro 1.2 software, enabling the evaluation of the fraction and size distribution of grains present in the sample.

2.5. Hardness testing

For the microhardness testing, a Shimadzu HMV-G microhardness tester was employed, equipped with a square based diamond indenter with a 136° angle between opposite faces. Sample preparation was performed as described in Section 2.4. For this study, 11 indentations were carried out along the cross section of the material, oriented at 90° relative to the deposition substrate, with an applied load of 9.807 N and an indentation spacing of 1.0 mm.

2.6. X-ray diffraction

Mineralogical phase composition was determined by X-Ray Diffraction (XRD) using a Shimadzu LabX XRD-6100 diffractometer. Phase identification was accomplished by comparing the obtained diffractograms with reference patterns contained in the Crystallography Open Database (COD 2018), employing the Match! 3 software. The results were obtained from the XRD analysis with the identified phases, with data processing performed using Origin 2019 Professional software.

3. Results and Discussions

In the following section, the results obtained throughout this study will be presented and discussed. Given that this represents a novel manufacturing technique, the experimental approach was designed to encompass a significant number of tests, with the purpose of generating a comprehensive set of results and thereby enabling a well-founded conclusion regarding the process.

3.1. Obtaining test samples

Figure 3 illustrates the wall obtained by additive manufacturing, in which the wall was deposited using both ER310 and ER70S-6 consumables, with both filler wires melted simultaneously into the same melt pool. Two walls were produced: one with an effective height of 100 mm and the other with an effective height of 45 mm. Both walls exhibited a total mean width of 11 mm and an effective mean width of 7.7 mm, yielding a mean layer height of 1.1 mm per layer.

3.2. Optical emission spectrometry tests

Table 2 presents the chemical composition of the ER310 and ER70S-6 consumables according to their respective standards, as well as the composition of the material following the WAAM process.

Spectrometric analysis of the sample reveals a resulting composition governed by the balance between the ER310 and ER70S-6 filler wires, directly reflecting the effects of dual-wire deposition. A significant reduction in chromium (18.03%) and nickel (14.89%) contents is observed relative to the ER310 alloy, while elements such as silicon (0.62%) and manganese (1.37%) assume intermediate values between the two consumables employed. Elements such as carbon and phosphorus exhibit contents consistent with the mixture of the filler materials, without pronounced deviations.

Recent literature demonstrates that variations in the chemical composition of deposited metals in GTAW processes involving dissimilar materials particularly the reduction of Cr and Ni are direct consequences of dilution, diffusion, and segregation phenomena occurring during WAAM.

In this context, the use of dual-wire feeding intensifies the mixing effect within the molten pool, making the material balance a determining factor in the final composition. Dilution promote the incorporation of elements originating from the lower alloyed wire (ER70S-6), resulting in the reduction of alloying elements characteristic of ER310, such as Cr and Ni[39]. Recent studies on GTAW indicate that the composition of the deposited metal may differ substantially from the nominal values due to this interaction between dissimilar alloys, particularly when austenitic materials and carbon steels are combined[40].

Furthermore, in WAAM processes, multiple thermal cycles and elevated heat inputs intensify both dilution and elemental redistribution, amplifying these compositional variations[41]. During solidification, interdendritic segregation of elements such as C and P may also occur, promoting local heterogeneities even when the overall composition adequately reflects the balance between the filler materials[42].

3.3. Tensile tests

As can be observed in the stress-strain curves presented in Figure 4, the studied specimens exhibit a ductile mechanical behavior.

Table 3 presents the results of ultimate tensile strength and yield strength, providing a comparison with the literature, where the authors in[43] conducted a study on ER310 stainless steel deposited by WAAM, and the authors in[44] investigated WAAM using ER70S-6 consumable.

Figure 3. Metallic wall obtained by AM through the GTAW-WAAM process, evidencing the layer-by-layer formation and the final geometry of the deposited structure.
Source: Author (2026).

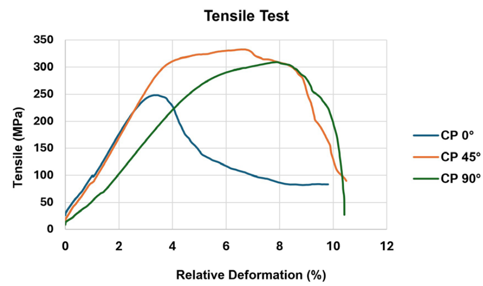

Figure 4. Results of mechanical tensile testing, presenting the stress-strain curves and mean values obtained for specimens oriented at 0°, 45°, and 90° relative to the deposition substrate, enabling the evaluation of the mechanical anisotropy of the material produced by additive manufacturing.
Source: Author (2026).

Table 2. Chemical composition of the material following AM processing, indicating the main elements present and their respective mass fractions, based on the analysis of the deposited material.

Element	AWS SFA 5.9 ER 310 Mass content (%) [a]	AWS A5.18 ER70S-6 Mass content (%)	Sample after AM Mass content (%)
C	0.08 – 0.15	0.06 – 0.15	0.092
Si	0.30 – 0.65	0.80 – 1.15	0.620
Mn	1.00 – 2.50	1.40 – 1.85	1.370
P	< 0.03	< 0.025	0.026
S	< 0.03	< 0.035	0.010
Cr	25.00 – 28.00	< 0.15	18.03
Mo	< 0.75	< 0.15	0.166
Ni	20.00 – 22.50	< 0.15	14.89
Cu	< 0.75	< 0.50	0.278
Fe	Balance for sum = 100%		

Source: Author (2026).

Table 3. Results of mechanical tensile testing of the material produced by additive manufacturing, including mechanical properties obtained for different orientations relative to the deposition substrate (0°, 45°, and 90°), with comparison to the strength of materials manufactured separately as reported in the literature.

Tests	Average ultimate tensile strength δ Máx. [MPa]	Average yield stress δe [MPa]	Elongation (%)	Standard deviation
Tensile 0º	248.5	229.2	≈ 9.7	45
Tensile 45º	333.0	287.7	≈ 10.3	15.2
Tensile 90º	309.4	230.3	≈ 10.4	5.1
ER310 Tensile 0º	320	198	≈ 12.5	4.1
ER310 Tensile 45º	419	280	≈ 11.5	12.6
ER310 Tensile 90º	430	269	≈ 15	12
ER70S-6 Tensile 0º	393.4	242.7	≈ 12	23.2
ER70S-6 Tensile 45º	399.3	277.3	≈ 13	41.3
ER70S-6 Tensile 90º	437.9	243.4	≈ 15	6.8

Source: Author (2026).

The tensile test results obtained for the component manufactured by GTAW-AM with dual ER310 + ER70S-6 wire feeding reveal a clearly heterogeneous and orientation dependent behavior (0°, 45°, and 90°), which is consistent with the intrinsically anisotropic nature of this type of additive process. Directional solidification and columnar grain growth along the deposition direction promote microstructural differences between regions parallel and perpendicular to the deposited layers, resulting in variations in ultimate tensile strength associated with the loading orientation. Recent studies demonstrate that materials produced by WAAM exhibit significant variations in mechanical properties as a function of direction, particularly due to the presence of interlayer interfaces, thermal heterogeneity, and chemical segregation factors that reduce strength when the load is applied transversely to the deposited layers[45].

In the specific case of deposition with dissimilar consumables, the mixing between ER310 and ER70S-6 intensifies microstructural and chemical heterogeneity, promoting deformation incompatibility between regions and favoring failure nucleation at interfaces, which contributes to the reduction of ultimate tensile strength compared to materials produced with single filler wires. Recent works involving dual-wire feeding in arc-based processes indicate that, although advantageous property combinations can be achieved, the presence of multiphase microstructures and compositional gradients tends to reduce ultimate strength relative to equivalent homogeneous materials, due to stress concentration and reduced interfacial cohesion[46]. Therefore, the reduction in strength observed relative to individual ER310 and ER70S-6 deposits should not be interpreted as an isolated performance loss, but rather as a direct consequence of the microstructural complexity and process induced anisotropy, being consistent with the expected behavior of multi-material WAAM systems.

3.4. Vickers microhardness tests

Figure 5 presents the HV profile measured perpendicular to the deposition layers of the manufactured sample. The hardness profile was obtained along a direction perpendicular to the deposited layers.

The mean HV value obtained for the sample was approximately 233 ± 20 HV. This hardness level is characteristic of stainless steels, owing to their high Cr and Ni contents, which contribute to resistance against impact and abrasive wear, in addition to preserving their mechanical properties at elevated temperatures. Table 4 presents a comparison of the mean hardness of the sample with values reported in the literature, where the authors in[4,44] conducted their research on WAAM with ER310 stainless steel consumable and WAAM with ER70S-6 alloy, respectively.

The higher mean hardness observed (233 ± 20 HV) in the sample produced by GTAW-WAAM with dual ER310 + ER70S-6 wire feeding can be more rigorously explained by the superposition of microstructural mechanisms induced by the process and by the hybrid composition. Recent studies indicate that, in GTAW-based WAAM processes, the introduction of alloying elements and chemical heterogeneity lead to significant microstructural variations, with a direct impact on hardness, particularly in alloys containing austenite rich in Cr and Ni, which exhibit greater hardness and variability when compared to low-carbon steels[45]. In the case of dissimilar material systems, the interaction between the carbon originating from ER70S-6 and the high Cr contents of ER310 favors solid solution hardening and the possible formation of hard secondary phases, such as carbides a mechanism already widely associated with hardness increase in materials fabricated by WAAM with chemical reinforcement[47]. Furthermore, the repeated thermal cycles characteristic of the process promote local microstructural refinement and interlayer heterogeneity, factors that also contribute to increased resistance to plastic deformation. Therefore, the superior hardness value does not derive solely from the presence of alloying elements, but from the synergy between the dissimilar composition, complex microstructural evolution, and the thermal history of the process, resulting in a microstructure exhibiting greater hardness than those reported for homogeneous reference materials.

3.5. Metallography

Figure 6 presents the metallographic analysis of the manufactured component.

The microstructure obtained by AM via GTAW with dual-wire feeding (ER310 + ER70S-6) exhibits features typical of WAAM processes, being markedly influenced by directional solidification mechanisms and the successive thermal cycles inherent to the process. The formation of regions with columnar dendritic morphology, oriented according to the heat flow direction, is observed, coexisting with areas of coarse equiaxed grains.

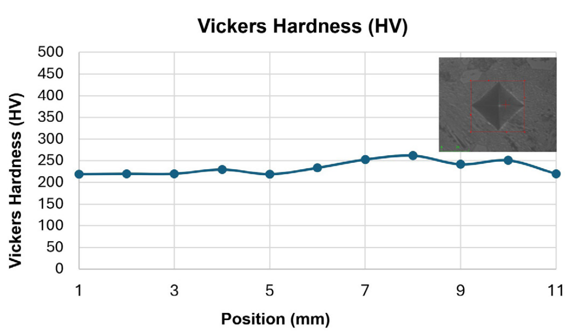

Figure 5. Distribution of Vickers hardness (HV) values obtained in the material produced by additive manufacturing, evidencing the variation in hardness along the analyzed regions and enabling the evaluation of the mechanical homogeneity of the deposited structure.

Source: Author (2026).

Table 4. Vickers hardness (HV) results of the material produced by additive manufacturing, in comparison with values reported in the literature for reference materials, enabling the evaluation of mechanical performance and the influence of the deposition process on hardness properties.

Sample	Average Hardness (HV)	Standard Deviation
ER310 + ER 70S-6	233	20
ER 310	191	8
ER 70S-6	161	23.7

Source: Author (2026).

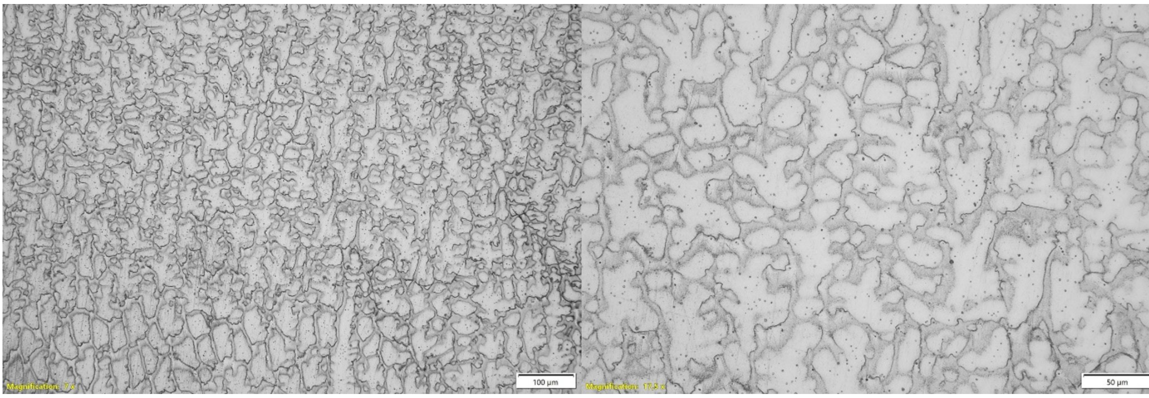

Figure 6. Metallographic microstructure of the consumable of the manufactured component, obtained after etching with Vilella's reagent, evidenced at magnifications of 200× and 500×, highlighting the microstructural features resulting from the additive manufacturing process.
Source: Author (2026).

Table 5. Results of grain size measurements of the sample produced by additive manufacturing, obtained by metallographic analysis, enabling the evaluation of the grain size distribution and the influence of the deposition process on the material microstructure.

Standard	ASTM E112-13[51]
Grain Size Number G	14.0
Mean Grain (μm)	3.04
Total Number of Grains	5715
Elongation	0.94
Fraction of Second Phase (%)	24.57
Image Ampliation	1000x

Source: Author (2026).

This microstructural heterogeneity is directly associated with local variations in thermal gradient and solidification rate, as well as the interlayer reheating effect.

The presence of refined columnar structures indicates conditions of high thermal gradient and moderate growth rate, favoring epitaxial growth along the deposited layers. On the other hand, regions exhibiting a more equiaxed morphology suggest a reduction in the local thermal gradient and/or intensification of heterogeneous nucleation phenomena, frequently induced by disturbances in the molten pool or by subsequent thermal cycles. This behavior is widely reported in the literature for WAAM processes, in which layer overlapping promote alternation between primary solidification zones and thermally affected regions from subsequent passes[48-50].

The use of dissimilar filler wires plays a central role in the observed microstructural evolution. Dilution between the austenitic stainless steel ER310 (rich in Cr and Ni) and the low-carbon steel ER70S-6 results in an intermediate chemical composition, as evidenced by the significant reduction in Cr and Ni contents. This compositional modification shifts the phase equilibrium, reducing austenite stability and favoring the formation of ferritic phases, particularly in interdendritic regions. As a consequence, the final microstructure tends to exhibit a partially austenitic matrix containing interdendritic ferrite and, possibly, acicular or bainitic constituents, depending on the local cooling conditions.

With the aim of characterizing the grain size of the microstructure, quantitative measurements were performed from the obtained micrographs. The results are presented in Table 5, which summarizes the grain size values determined for the sample.

Quantitative grain size analysis, performed in accordance with ASTM E112-13[51], revealed a grain size number G equal to 14, corresponding to a mean grain size of approximately 3.04 μm. This result indicates the formation of a significantly refined microstructure in the AM sample, particularly when compared to values reported in the literature for austenitic stainless steels obtained by conventional processing routes or even by additive processes.

According to the author in[52], upon analyzing 316L stainless steel, a mean grain size of 31 ± 2 μm was obtained, a value considerably larger than that observed in the present study. This difference demonstrates that the dual-wire AM process (ER310 + ER70S-6), combined with the thermal conditions imposed by GTAW-based WAAM, promoted microstructural refinement. This behavior can be attributed to the high local solidification rate and the repetition of thermal cycles, which promote dendritic fragmentation and nucleation of new grains, resulting in a finer microstructure.

Furthermore, as discussed by[53], materials with refined grain size exhibit increased hardness and improved mechanical properties, since grain size reduction acts as a barrier to dislocation motion (Hall-Petch effect). Although severe plastic deformation processes can lead to submicrometric grain sizes (< 1 μm), as mentioned by the author, the values obtained in the present study (approximately 3 μm) already indicate a significant level of refinement for materials processed via fusion-based routes.

The observed second phase fraction (24.57%) also suggests the presence of microstructural heterogeneities arising from non-equilibrium solidification and dilution between the dissimilar materials. This condition may additionally contribute to the effective microstructural refinement, as phase interfaces act as barriers to grain growth.

Overall, the results presented in Table 5 indicate that the employed AM process not only promoted the formation of a heterogeneous microstructure, but also resulted in significant grain size refinement compared to literature data, which may positively impact the mechanical properties of the deposited material.

3.6. SEM, EDS, and mapping analysis

SEM-EDS analyses were performed to examine the inclusions originating from the process. Figure 7 presents the image obtained by SEM referring to the microstructure of the sample, highlighting point A, where point spectrometry was conducted at the grain boundary.

Figure 8 presents the chemical composition spectrum at the grain boundary intersection point, identifying the energy peak of each element present at the analysis point.

Table 6 presents the chemical composition obtained at the point within an inclusion and at the intersection point between the grain and the grain boundary.

Table 6 presents the point chemical composition obtained by EDS for the regions indicated in Figure 7 (point A) and Figure 8 (point B). In both analyzed points, the predominance of Fe is observed, followed by significant Cr contents and smaller amounts of Ni. This distribution is consistent with the overall composition of the deposited material, previously discussed, which results from the dilution between the ER310 and ER70S-6 filler wires.

Table 6. Point chemical composition of the inclusion analyzed by energy-dispersive spectroscopy (EDS), presenting the identified elements and their respective mass fractions, with the purpose of characterizing the chemical nature of the inclusion present in the material.

Element	Point A Mass fraction (%)	Point B Mass fraction (%)
Cr	21.79	20.93
Ni	3.08	1.07
Fe	75.13	78.00

Source: Author (2026).

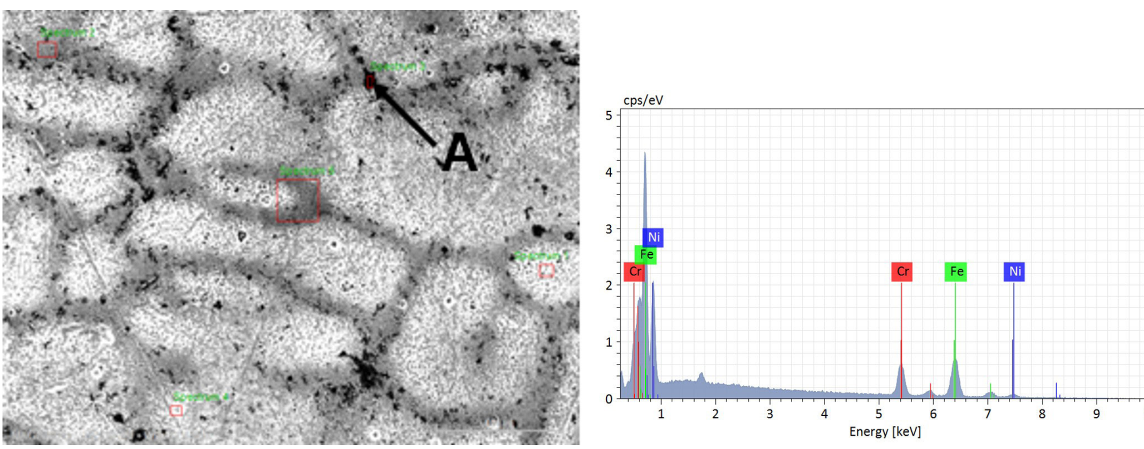

Figure 7. Image obtained by scanning electron microscopy (SEM) at a magnification of 1500×, associated with the point chemical composition spectrum by EDS identified at point A, evidencing the presence and distribution of the constituent elements of the analyzed phase.

Source: Author (2026).

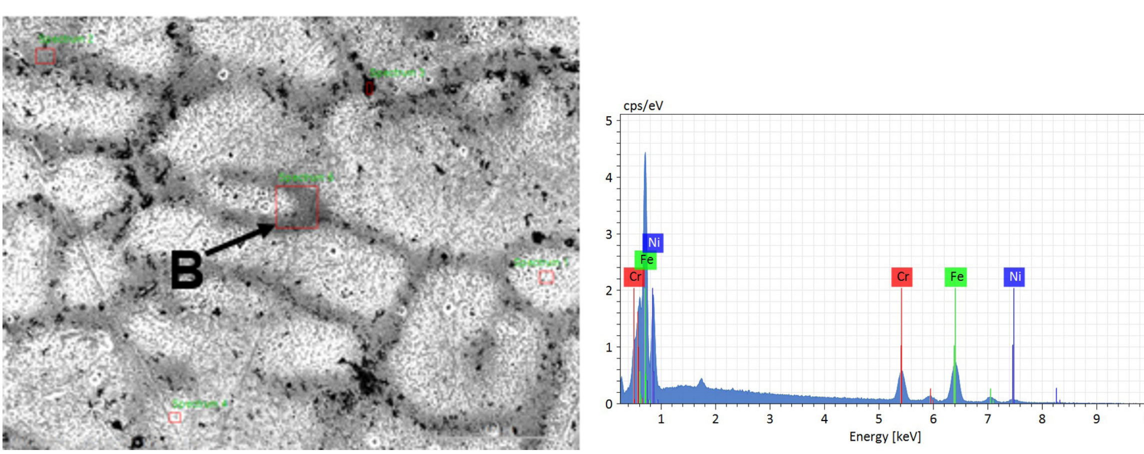

Figure 8. Image obtained by scanning electron microscopy (SEM) at a magnification of 1500×, associated with point chemical composition analysis by EDS at the intersection region between the grain and the grain boundary, indicated at point B, evidencing the elemental distribution at this microstructural interface.

Source: Author (2026).

EDS analyses performed at the highlighted regions indicate that both intragranular areas and regions adjacent to grain boundaries present a composition based on the Fe–Cr–Ni system, without abrupt chemical variations between points A and B. However, a slight reduction in Ni content and a relative increase in Fe is noted at point B, located in a region associated with the grain boundary, which may be related to local segregation effects during solidification.

Accordingly, the analyzed regions can be interpreted as microstructural heterogeneities associated with non-equilibrium solidification and elemental redistribution during the thermal cycles of the WAAM process, rather than as distinct precipitates. This behavior is consistent with the literature, in which deposits obtained by arc-based AM in Fe–Cr–Ni alloys tend to exhibit microstructures dominated by austenitic solid solution (γ), with possible local compositional variations arising from micro segregation[54].

According to the author in[54], analyses of metals deposited with similar alloys (such as ER307) reveal the predominance of the γ phase (austenite), a solid solution based on the iron nickel chromium system with a Face Centered Cubic (FCC) crystal structure. The diffraction peaks observed in these studies are consistent with results previously reported for austenitic stainless steels produced by arc AM, reinforcing the interpretation that the microstructure of the analyzed material is predominantly governed by this phase.

Figures 9 and 10 present the elemental maps obtained by EDS for the sample produced by GTAW-AM with dual-wire feeding (ER310 + ER70S-6). Overall, a relatively homogeneous distribution of the main alloying elements (Fe, Cr, Ni, C, Si, and Cu) is observed, with no evidence of macroscopic segregation or well-defined compositional banding at the analyzed scale.

This apparent homogeneity can be attributed to the efficient metallurgical mixing within the melt pool, intensified by the use of dual-wire feeding, as well as by the successive thermal cycles characteristic of the WAAM process. Interlayer remelting promote elemental redistribution and the smoothing of chemical gradients, resulting in locally stabilized compositions after multiple passes. This behavior is consistent with the literature, which reports significant diffusion of elements such as Cr and Ni in dissimilar systems processed by WAAM, leading to regions with progressively more uniform composition[48,55].

It is worth noting that, although the maps indicate homogeneity at the micrometric scale and at the magnification employed, this does not exclude the existence of micro segregation at a finer (submicrometric) scale, unresolved by the technique under the conditions used. Nevertheless, the absence of abrupt compositional variations suggests that the thermal regime adopted favored effective mixing between the filler materials, resulting in behavior approaching that of an in situ formed alloy.

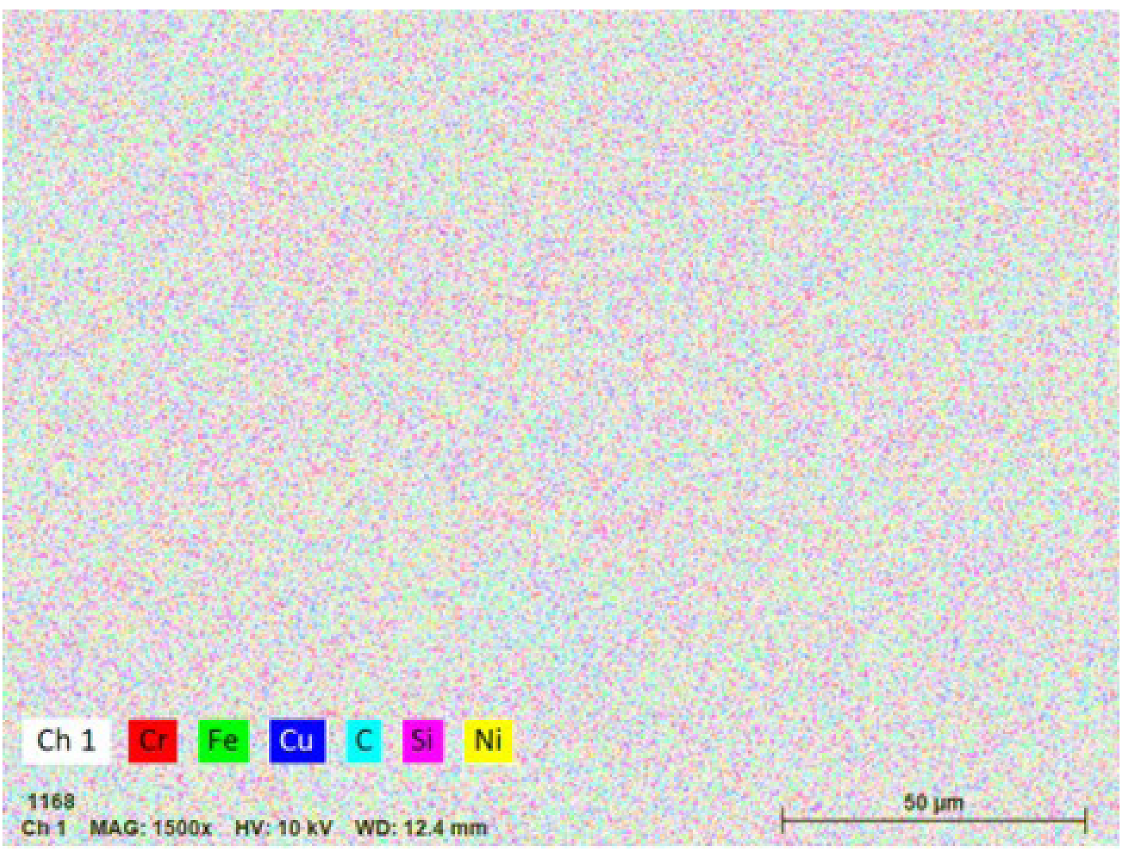

Figure 9. Elemental mapping of the sample obtained by energy-dispersive spectroscopy (EDS), evidencing the spatial distribution of the chemical elements present and enabling the compositional evaluation of the analyzed material.

Source: Author (2026).

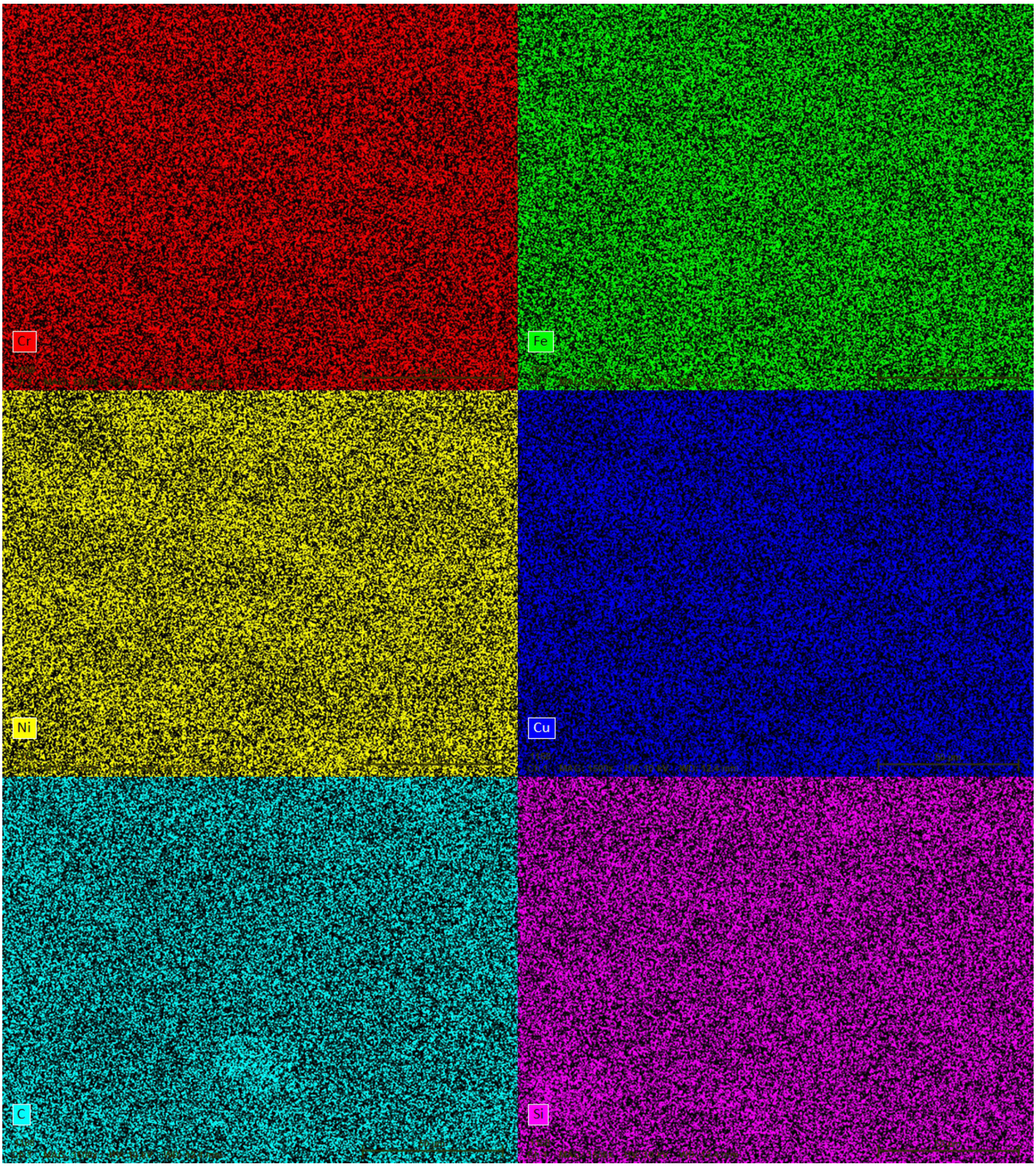

Figure 10. Image obtained by scanning electron microscopy (SEM), accompanied by the results of elemental mapping by energy-dispersive spectroscopy (EDS), presented separately, evidencing the distribution of the main chemical elements in the analyzed region.

Source: Author (2026).

Additionally, unlike the previous point analyses, the elemental mapping allowed the identification of carbon distributed throughout the matrix, albeit in a diffuse manner, which is associated with the detection limitations of this element by EDS in localized analyses. Taken together, the results indicate that the process promoted a microstructure with low chemical heterogeneity at the observed scale.

3.7. X-ray diffraction (XRD)

Figure 11 presents the XRD analysis result of the sample, in which the presence of carbides of the $Cr_{0 \cdot 8}Ni_{0 \cdot 2}$ type can be observed.

XRD analysis indicated the formation of the $Cr_{0 \cdot 8}Ni_{0 \cdot 2}$ alloy as a Cr-rich substitutional solid solution, retaining the Body Centered Cubic (BCC) crystal structure characteristic of chromium. The absence of additional peaks associated with intermetallic phases or metallic Ni confirms the formation of a single phase, indicating the structural homogeneity of the obtained alloy. The material is predominantly composed of iron with a BCC structure (α-Fe), evidenced by the highest intensity peak, suggesting that this is the majority phase and possibly exhibiting preferred orientation. The presence of a low-intensity secondary phase is also observed, attributed to a chromium rich nitride, indicating a reduced volumetric fraction of this phase.

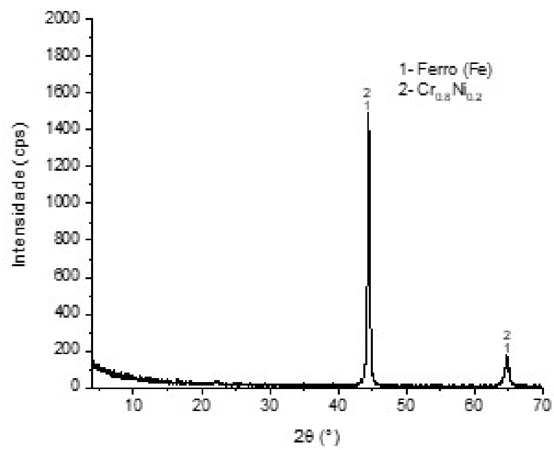

Figure 11. X-ray diffraction (XRD) result of the sample produced by additive manufacturing, presenting the diffractogram with identification of the crystalline phases present and enabling the structural analysis of the deposited material.

Source: Author (2026).

The well-defined and narrow diffraction peaks reveal high crystallinity and negligible amorphous phase content.

The authors in[56], in their research on the microstructure of welded AISI 310 steels, highlight that XRD analysis allows the identification of characteristic peaks of austenite, ferrite, sigma phase, and $M_{23}C_6$ precipitates. These results are consistent with the literature; however, due to peak overlapping, additional analyses are required for conclusive identification.

4. Conclusions

The present experimental investigation demonstrated the potential of WAAM-based AM employing the GTAW process with dual-wire feeding (ER310 + ER70S-6), evidencing the viability of co-deposition within a single melt pool with adequate process stability and metallurgical integrity of the produced material.

Chemical analysis indicated that the final composition of the material is strongly influenced by dilution between the consumables, resulting in a reduction of alloying element contents characteristic of ER310, such as Cr and Ni, and in an intermediate composition typical of dissimilar material systems. This behavior confirms the predominant role of material balance and melt pool dynamics in defining the final composition.

Tensile test results evidence the anisotropic behavior of the material produced by GTAW-AM with dual-wire feeding (ER310 + ER70S-6), with properties dependent on the orientation relative to the deposited layers. The mean ultimate tensile strength ranged from 248.5 MPa (0°) to 333.0 MPa (45°) and 309.4 MPa (90°), while the yield strength presented values of 229.2 MPa (0°), 287.7 MPa (45°), and 230.3 MPa (90°). Superior mechanical performance was observed at the intermediate orientation (45°), suggesting a more favorable stress distribution condition relative to the columnar morphology and interlayer interfaces. When compared to individually deposited materials reported in the literature, the obtained values are generally lower than those of ER310 and ER70S-6, which exhibit higher ultimate tensile strengths (up to 430 MPa) and greater elongation. This reduction is attributed to the dissimilar nature of the material, in which inter-alloy dilution, combined with the presence of compositional gradients and microstructural heterogeneities, promote local deformation incompatibilities and favors failure nucleation.

From a microstructural standpoint, the sample exhibited significant grain refinement, with a mean grain size of approximately 3.04 µm (G = 14), a value substantially lower than those reported in the literature for austenitic stainless steels processed by conventional routes. This refinement is associated with the high solidification rates and repeated thermal cycles of the WAAM process, which favor nucleation and limit grain growth.

Microhardness results indicated a relatively homogeneous profile along the analyzed cross-section, evidencing microstructural consistency of the deposited material. The obtained values were superior to those typically reported for 310 stainless steels, which may be associated with microstructural refinement and the presence of local heterogeneities arising from non-equilibrium solidification and the mixing between dissimilar alloys.

SEM, EDS, and elemental mapping analyses confirmed the distribution of the main alloying elements (Fe, Cr, and Ni) at the micrometric scale, with no evidence of macroscopic segregation. The elemental mapping also allowed the identification of carbon distributed throughout the matrix, albeit in a diffuse manner. These results indicate that the successive thermal cycles and interlayer remelting promoted efficient metallurgical mixing, resulting in a microstructure with low chemical heterogeneity at the analyzed scale.

Overall, the obtained results indicate that the dual-wire deposition strategy via GTAW can be employed for the production of dissimilar materials, constituting a viable alternative for applications requiring compositional control and enhanced mechanical properties.

5. Acknowledgments

The authors would like to express their gratitude to Centro Universitário UNISATC for supporting the research through the use of its laboratory facilities, and to the Fundação de Amparo à Pesquisa e Inovação do Estado de Santa Catarina (FAPESC) for the financial support provided for the procurement of research equipment and supplies.

6. Data Availability

The dataset that supports the findings of this study is fully available within the article.

7. References

1. Dagostim DK, Daleffe A, Casagrande HC, March G, Ferreira CA, Schaeffer L, et al. Desenvolvimento do processo de manufatura aditiva com deposição localizada através da tecnologia GMAW duplo arame. Obs Econ Latinoam. 2024;22(10):e7351. https://doi.org/10.55905/oelv22n10-185.
2. Bonifácio DC, Milanez A, Daleffe A, Possamai PHM, Casagrande HC, De March G. Determinação de lote mínimo para viabilização de uma célula para soldagem robotizada em uma indústria de implementos. Vincci. 2025;9(2):205-25. https://doi.org/10.70185/2525-6025.2024.v9.407.

3. Casagrande HC, Daleffe A, Martins H, De March G, Milanez A, Possamai PHM, et al. Caracterização microestrutural e de microdureza para o arame tubular UTP AF LEDURIT 60 impresso atraves da tecnica de manufatura aditiva por arco eletrico. Vincci. 2024;9(2):622-38. https://doi.org/10.70185/2525-6025.2024.v9.422.
4. De March G, Daleffe A, Casagrande HC, Ferreira CA, Schaeffer L, Milanez A. Manufatura aditiva por deposição a arco: estudo das propriedades mecânicas e quimicas com eletrodo inoxidavel ER 310. Rev Gest Soc Ambient. 2025;19(5):1-16.
5. Silva JV, Schaeffer L, Daleffe A, Milanez A, Casagrande HC, De March D. Analysis of the bimetallic joint of a hot-forged crosshead composed of ASTM B221 6060 aluminum and AWS A5.36 E110C-G M low alloy steel obtained by localized fusion additive manufacturing. Mater Res. 2025;28:e20250347. https://doi.org/10.1590/1980-5373-MR-2025-0347.
6. Pattanayak S, Sahoo SK. Gas metal arc welding based additive manufacturing a review. CIRO J Manuf Sci Technol. 2021;33: 398-442. https://doi.org/10.1016/j.cirpj.2021.04.010.
7. Costa TE, Resende AA. Manufatura aditiva por deposição a arco (MADA): tendências recentes e futuras perspectivas. In: Simpósio de Engenharia de Produção; 2024; Catalão, GO. Anais. Catalão: Universidade Federal de Catalão; 2024.
8. Cunningham CR, Flynn JM, Shokrani A, Dhokia V, Newman ST. Invited review article: strategies and processes for high quality wire arc additive manufacturing. Addit Manuf. 2018;22:672-86. https://doi.org/10.1016/j.addma.2018.06.020.
9. Casagrande HC, Daleffe A, Ferreira CA, Fritzen D, De March G, Castelan J. Processo de fabricação de peças metálicas por manufatura aditiva com fusão localizada de aços baixa liga. Open Sci Res XI. 2023;11:997-1008. https://doi.org/10.37885/230512991.
10. Gain S, Singh M, Ghorpade A, Singh RKR, Singh PK. Microstructural integrity and mechanical synergy at the ER2205-Inconel 718 interface in functionally graded wire arc additively manufactured bimetallic structures. Mater Today Commun. 2026;52:114983. https://doi.org/10.1016/j.mtcomm.2026.114983.
11. Paskual A, Álvarez P, Suárez A. Study on arc welding processes for high deposition rate additive manufacturing. Procedia CIRP. 2018;68:358-62. https://doi.org/10.1016/j.procir.2017.12.095.
12. Novelino ALB, Carvalho GC, Reis RP, Ziberov M. Métodos para manufatura aditiva de metais a arco eletrico: uma revisão. In: 11º Congresso Brasileiro de Engenharia de Fabricação; 2021; Curitiba, PR. Anais. Rio de Janeiro: ABCM; 2021.
13. Ferreira CA, Daleffe A, Casagrande HC, De March G, Martins H, Schaeffer L. Análise mecânica do arame ER70S-6 em manufatura aditiva pulsada. Rev Gest Prod Oper Sist. 2025;19:1-13.
14. Farias RM, Vilarinho LO. Computational simulations of metal additive manufacturing processes: an introductory review. Uberlândia: Faculdade de Engenharia Mecânica, Universidade Federal de Uberlandia; 2022.
15. Wang D, Zhang S, Hu R, Wang W, Hu S, Liu F, et al. Pulsed TIG wire arc additive manufactured 17-4 PH stainless steel: effect of Cu-rich precipitates and δ-ferrite on the mechanical properties. Mater Sci Eng A. 2024;912:146972. https://doi.org/10.1016/j.msea.2024.146972.
16. Lyu Z, Sato YS, Xu W, Li S, Xu Z, Hu X, et al. Simultaneous enhancements of strength and ductility of wire arc additive manufactured 17-4PH steel via intrinsic heat treatment. J Mater Process Technol. 2023;321:118149. https://doi.org/10.1016/j.jmatprotec.2023.118149.
17. Ferreira CA, Casagrande HC, Daleffe A, Fritzen D, De March G, Schaeffer L. Fabricação de peças metálicas por manufatura aditiva com diferentes características mecânicas superficiais. Rev Gest Secr. 2024;15(7):1-15. https://doi.org/10.7769/gesec.v15i7.3850.
18. Singh S, Ramakrishna S, Singh R. Material issues in additive manufacturing: a review. J Manuf Process. 2017;25:185-200. https://doi.org/10.1016/j.jmapro.2016.11.006.
19. Rodrigues VP, Zancul ES, Mançanares CG, Giordano MS, Salerno MS. Manufatura aditiva: estado da arte e framework de aplicações. Rev Gest Prod Oper Sist. 2017;12(3):1-34. https://doi.org/10.15675/gepros.v12i3.1657.
20. Song Y, Park S, Choi D, Jee H. 3D welding and milling: part I–a direct approach for freeform fabrication of metallic prototypes. Int J Mach Tools Manuf. 2005;45(9):1057-62. https://doi.org/10.1016/j.ijmachtools.2004.11.021.
21. Liu J, To AC. Quantitative texture prediction of epitaxial columnar grains in additive manufacturing using selective laser melting. Addit Manuf. 2017;16:58-64. https://doi.org/10.1016/j.addma.2017.05.005.
22. Theriault A, Xue L, Dryden JR. Fatigue behavior of laser consolidated IN-625 at room and elevated temperatures. Mater Sci Eng A. 2009;516(1-2):217-25. https://doi.org/10.1016/j.msea.2009.03.056.
23. Khan AU, Sadhya A, Kumar AB, Chatterjee S, Madhukar YK. Investigation on dual-wire TIG Arc additive manufacturing of IN625 and SS316L FGM for continuous gradient and sandwich structures. Thin Walled Struct. 2024;200:111881. https://doi.org/10.1016/j.tws.2024.111881.
24. Pinomaa T, Lindroos M, Walbruhl M, Provatas N, Laukkanen A. The significance of spatial length scales and solute segregation in strengthening rapid solidification microstructures of 316L stainless steel. Acta Mater. 2020;184:1-16. https://doi.org/10.1016/j.actamat.2019.10.044.
25. Chernovol N, Lauwers B, van Rymenant P. Development of low-cost production process for prototype components based on Wire and Arc Additive Manufacturing (WAAM). Procedia CIRP. 2020;95:60-5. https://doi.org/10.1016/j.procir.2020.01.188.
26. Lima EH, Souza DDBG, Fernandes DB, Vitorino BG, Vilarinho LO. Viabilidade operacional da fabricação de peças em aço carbono em manufatura aditiva por deposição a arco fazendo uso de duplo arame. In: 47º Congresso Nacional de Soldagem (XLVII CONSOLDA); 2025; Joinville, SC. Anais. Recife: Even3; 2025.
27. Mohan Kumar S, Rajesh Kannan A, Pravin Kumar N, Pramod R, Siva Shanmugam N, Vishnu AS, et al. Microstructural features and mechanical integrity of wire arc additive manufactured SS321/Inconel 625 functionally gradient material. J Mater Eng Perform. 2021;30(8):5692-703. https://doi.org/10.1007/s11665-021-05617-3.
28. Ahsan MRU, Tanvir ANM, Ross T, Elsawy A, Oh MS, Kim DB. Fabrication of bimetallic additively manufactured structure (BAMS) of low-carbon steel and 316L austenitic stainless steel with wire + arc additive manufacturing. Rapid Prototyping J. 2020;26(3):519-30. https://doi.org/10.1108/RPJ-09-2018-0235.
29. Ahsan MRU, Tanvir ANM, Seo G-J, Bates B, Hawkins W, Lee C, et al. Heat-treatment effects on a bimetallic additively-manufactured structure (BAMS) of the low-carbon steel and austenitic-stainless steel. Addit Manuf. 2020;32:101036. https://doi.org/10.1016/j.addma.2020.101036.
30. Chaturvedi M, Scutelnicu E, Rusu CC, Mistodie LR, Mihailescu D, Subbiah AV. Wire arc additive manufacturing: review on recent findings and challenges in industrial applications and materials characterization. Metals (Basel). 2021;11(6):939. https://doi.org/10.3390/met11060939.
31. Yang D, He C, Zhang G. Forming characteristics of thin-wall steel parts by double electrode GMAW based additive manufacturing. J Mater Process Technol. 2016;227:153-60. https://doi.org/10.1016/j.jmatprotec.2015.08.021.
32. Lu F, Yao S, Lou SN, Li YB. Modeling and finite element analysis on GTAW arc and aeld pool. Comput Mater Sci. 2004;29(3): 371-8. https://doi.org/10.1016/j.commatsci.2003.10.009.
33. Geng H, Li J, Xiong J, Lin X, Zhang FS. Optimization of wire feed for GTAW-based additive manufacturing. J Mater Process Technol. 2017;243:40-7. https://doi.org/10.1016/j.jmatprotec.2016.11.027.

34. Wang Z, Zhang Y. A review of aluminum alloy fabricated by different processes of wire arc additive manufacturing. Mater Sci. 2021;27(1):18-26.
35. Geng H, Li J, Xiong J, Lin X, Zhang FS. Optimization of wire feed for GTAW-based additive manufacturing. J Mater Process Technol. 2017;243:40-7. https://doi.org/10.1016/j.jmatprotec.2016.11.027.
36. Cizenski RP, Daleffe A, Ferreira CA, Shaeffer L. Manufatura aditiva na construção de peças metalicas para uso na industria cerâmica. Rev. Vincci. 2023;8(2):515-41. https://doi.org/10.70185/2525-6025.2023.v8.342.
37. Casagrande HC, Daleffe A, De March G, Ferreira CA, Silva JV, Martins H, et al. Precipitação de carbono na linha de ligação entre material depositado e material de base utilizando o processo de manufatura aditiva. Revista Científica Sistemática. 2024;2:733-46.
38. ASTM: American Society for Testing and Materials. ASTM E8: standard test methods for tension testing of metallic materials. West Conshohocken: ASTM; 2022.
39. Sonar T, Ivanov M, Trofimov E, Liu K, Shcherbakov I, Shaburova N, et al. A critical review on dissimilar welding of ferritic-martensitic steel and austenitic stainless steel using gas tungsten arc welding process: weldability issues, processing, and performance characteristics of joints. J Manuf Process. 2025;133:811-64. https://doi.org/10.1016/j.jmapro.2024.11.081.
40. Chuaiphan W, Kumkoon P, Kalnaowakul P. Dissimilar welding of AISI 201 and 202 low nickel stainless steels by GTA and PA welding processes. Journal of Alloys and Metallurgical Systems. 2023;4:100047. https://doi.org/10.1016/j.jalmes.2023.100047.
41. Nahmany M, Aghion E. A review of the latest welding technologies for metallic components produced by additive manufacturing processes. J Mater Eng Perform. 2026;35(13):12259-79. https://doi.org/10.1007/s11665-025-12472-z.
42. Schmidt J, Rust B, Stroetmann R. The influence of cooling on the alloy distribution in weld metals. Journal of Welding International. 2024;38(11):750-61. https://doi.org/10.1080/09507116.2024.2418913.
43. Cipriano A, Malfatti CF, Casagrande HC, Daleffe A, Castelan J, Possamai PHM. Analysis of the microstructure and mechanical properties of austenitic stainless steel 310 manufactured via WAAM. J Mater. 2025;18:16.
44. Possamai PHM, Daleffe A, Casagrande HC, Ferreira CA, Schaeffer L, Bilessimo LD. Estudo do processo de manufatura aditiva por fusão localizada para ligas E71T-1 e ER70S-6. Gest Soc Ambient. 2025;19(7):1-14.
45. Singh J, Il'yenko V, Oliveira JP. Comparative study of GTAW and GMAW for WAAM: microstructural and mechanical insights in ER70S-6 and 316L stainless steel depositions. Sci Technol Weld Join. 2025;30(3):220-30. https://doi.org/10.1177/13621718251353015.
46. Ayan Y. Fabrication and characterization of a new high-strength ally via WAAM using GMAW+cold wire feeding. Mater Chem Phys. 2024;328:130038. https://doi.org/10.1016/j.matchemphys.2024.130038.
47. Bayar I, Ulutan M. Investigation of microstructure and mechanical properties of SiC and FeCrC reinforced components fabricated with plasma wire arc additive manufacturing (P-WAAM). Mater Sci Eng A. 2023;875:145115. https://doi.org/10.1016/j.msea.2023.145115.
48. Zhai W, Aishwarya RS, Zhou W. Microstructure and mechanical properties of the wire arc additively manufactured 316L-ER70S-6 bimetal structure. J Virtual Phys Prototyp. 2014;19(1):e2375105.
49. Wu B, Pan Z, Ding D, Cuiuri D, Li H, Xu J, et al. A review of the wire arc additive manufacturing of metals: properties, defects and quality improvement. J Manuf Process. 2018;35:127-39. https://doi.org/10.1016/j.jmapro.2018.08.001.
50. Wang F, Williams S, Colegrove P, Antonysamy AA. Microstructure and mechanical properties of wire and arc additive manufactured TI-6Al-4V. Metall Mater Trans, A Phys Metall Mater Sci. 2013;44(2):968-77. https://doi.org/10.1007/s11661-012-1444-6.
51. ASTM: American Society for Testing and Materials. ASTM E112-13: standard test methods for determining average grain size. West Conshohocken: ASTM; 2021.
52. Demarque R, Silva RS, Santos EP, Castro JA. Avaliação de parâmetros de soldagem nas características de juntas dissimilares Inconel 718 - Inox 316L soldadas pelo processo TIG autógeno. Soldag Insp. 2018;23(3):380-92. https://doi.org/10.1590/0104-9224/si2303.07.
53. Rodrigues RS. Estudo da resistência a corrosão intergranular do aço inoxidável austenitico F138: perspectiva de desempenho após deformação plástica severa (DPS) [dissertação]. São Carlos: Universidade Federal de São Carlos; 2018.
54. Gunen A, Gurol U, Koçak M, Çam G. A new approach to improve some properties of wire arc additively manufactured stainless steel components: simultaneous homogenization and boriding. Surf Coat Tech. 2023;460:129395. https://doi.org/10.1016/j.surfcoat.2023.129395.
55. Yadav A, Srivastava M, Jain PK, Rathee S. Rathee. Microstruture and tribological behaviour of dissimilar steel functional structure developed via arc-based DED process. Tribol Int. 2024;197:109782. https://doi.org/10.1016/j.triboint.2024.109782.
56. Garcia JM, Nunes TS, Saber AFS, Sousa TG, Brandao LP. Efeitos do envelhecimento por fluência na microestrutura do aço AISI 310 soldado. In: 76º Congresso Anual da ABM Week; 2023; São Paulo, SP. Anais. São Paulo: ABM Brasil; 2023. (vol. 7).